Till, J., Cogné, J.-P., Marquer, D., Poilvet, J.-C. (2015): Magnetic fabric evolution in ductile shear zones: examples in metagranites of the Aar Massif (Swiss Central Alps). - *Terra Nova*, *27*, 3, pp. 184—194.

DOI: http://doi.org/10.1111/ter.12147

Terra Nova

doi: 10.1111/ter.12147

Magnetic fabric evolution in ductile shear zones: examples in metagranites of the Aar Massif (Swiss Central Alps)

Jessica L. Till,[1,2] Jean-Pascal Cogné[1] Didier Marquer[3] and Jean-Charles Poilvet[3]

[1]*Institut de Physique du Globe de Paris, Sorbonne Paris Cité, Univ. Paris Diderot, CNRS, F-75005 Paris, France;* [2]*Helmholtz-Zentrum Potsdam, Deutsches GeoForschungsZentrum (GFZ), Telegrafenberg, Potsdam 14473, Germany;* [3]*UMR 6249 Chrono-Environnement, Université de Franche-Comté, 16 route de Gray, Besançon Cedex F-25030, France*

ABSTRACT

The Aar Massif forms part of the polycyclic basement of the External Crystalline Massifs in central Switzerland. Strong heterogeneous Alpine deformation produced a network of broad, anastomosing shear zones, with deformation strongly localized in mylonitic domains. This study investigates the combined effects of high-strain deformation and synkinematic metamorphism on magnetic fabric evolution in Tertiary shear zones of the Aar granite and Grimsel granodiorite. In transects across several mesoscale shear zones with large strain gradients, magnetic fabric orientations are in excellent agreement with principal strain orientations determined from outcrop fabrics and strain markers. However, the magnitude and shape of the magnetic anisotropy do not change systematically with increasing finite strain, likely as a result of recrystallization and metamorphism. The overall pattern of steeply dipping fabrics is consistent with the main shortening stage of regional Alpine kinematics, while some mylonite structures reflect a local component of dextral shearing.

Terra Nova, 27, 184–194, 2015

Introduction

Anisotropy of magnetic susceptibility (AMS) has been utilized to study deformed rocks for many years (Graham, 1966; Tarling and Hrouda, 1993; Borradaile and Jackson, 2004). AMS is a sensitive and useful tool for tracking microstructural variations in deformed crystalline rocks where strain markers are often absent (e.g. Bouchez *et al.*, 1990; see review in Ferré *et al.*, 2014); however, some uncertainty remains about how various mineral strain responses and deformation mechanisms are reflected by bulk-rock magnetic anisotropy. In particular, the effects of synkinematic metamorphism on magnetic fabrics in deformed rocks are not well understood. We performed a magnetic fabric study in ductile metagranite shear zones of the Aar Massif to elucidate the variations in AMS across large strain gradients in rocks exposed to Alpine fluid-present greenschist-facies conditions. Comparing finite strain measurements and mineral microstructures with magnetic fabrics reveals complexities in the fabric evolution due to recrystallization and changes in mineralogy that accompanied deformation.

Correspondence: Dr. Jessica L. Till, Section 3.2, GeoForschungsZentrum Potsdam, Telegrafenberg, Potsdam 14473, Germany. Tel.: +49 (0)331 288 1322; e-mail: till@gfz-potsdam.de

Geological setting

Part of the External Crystalline Massifs (ECM) of the Swiss Central Alps, the Aar Massif is a large polycyclic pre-Variscan basement belonging to the Helvetic domain (Fig. 1A). During Tertiary Alpine continent-continent collision (Pfiffner *et al.*, 1990) the ECM was thrust towards the northwest under greenschist-facies metamorphic conditions (Steck, 1966, 1984; Choukroune and Gapais, 1983; Marquer *et al.*, 1985; Marquer, 1987). The Aar Massif consists of Palaeozoic gneisses, migmatites and amphibolites, which were intruded by several late-orogenic Variscan intrusives, including the Aar granite and the Grimsel granodiorite (Steck, 1966, 1984; Abrecht, 1994; Schaltegger, 1994). During Tertiary tectonics, heterogeneous deformation associated with bulk NW–SE shortening produced a network of anastomosing ductile shear zones surrounding lenses of less-deformed rocks (Choukroune and Gapais, 1983; Marquer *et al.*, 1985; Gapais *et al.*, 1987; Fig. 1B and C). The Alpine schistosity and the shear-zone patterns of the Aar and Gotthard Massifs were analysed on a large scale by Choukroune and Gapais (1983) and Marquer (1990). They interpreted the sub-vertical alpine schistosity and the sub-vertical stretching lineation in the cores of both massifs to result from bulk coaxial NW–SE horizontal shortening during thrusting of the ECM.

The metamorphic conditions associated with this main Tertiary ductile deformation are estimated at around 450 ± 25 °C and 0.65 ± 0.1 GPa during Oligo-Miocene times in the Grimsel granodiorite (Challandes *et al.*, 2008 and references therein; Goncalves *et al.*, 2012, 2013). Mineralogical changes associated with chemical mass-transfer related to large-volume fluid circulation occurred during the formation of these ductile shear zones (Marquer *et al.*, 1985; Marquer and Peucat, 1994; Goncalves *et al.*, 2012, 2013) under largely isovolumetric conditions (Fourcade *et al.*, 1989). The three sampled high-strain zones are located in the Grimsel granodiorite and the Aar granite (Fig. 1B and C). The studied ductile shear zones progressively evolve from weakly deformed protolith (Aar granite and Grimsel granodiorite) to orthogneiss and mylonite along decametre-scale strain gradients. Although the main stage of NW–SE compressional deformation in the Alps was followed by lateral movement, producing

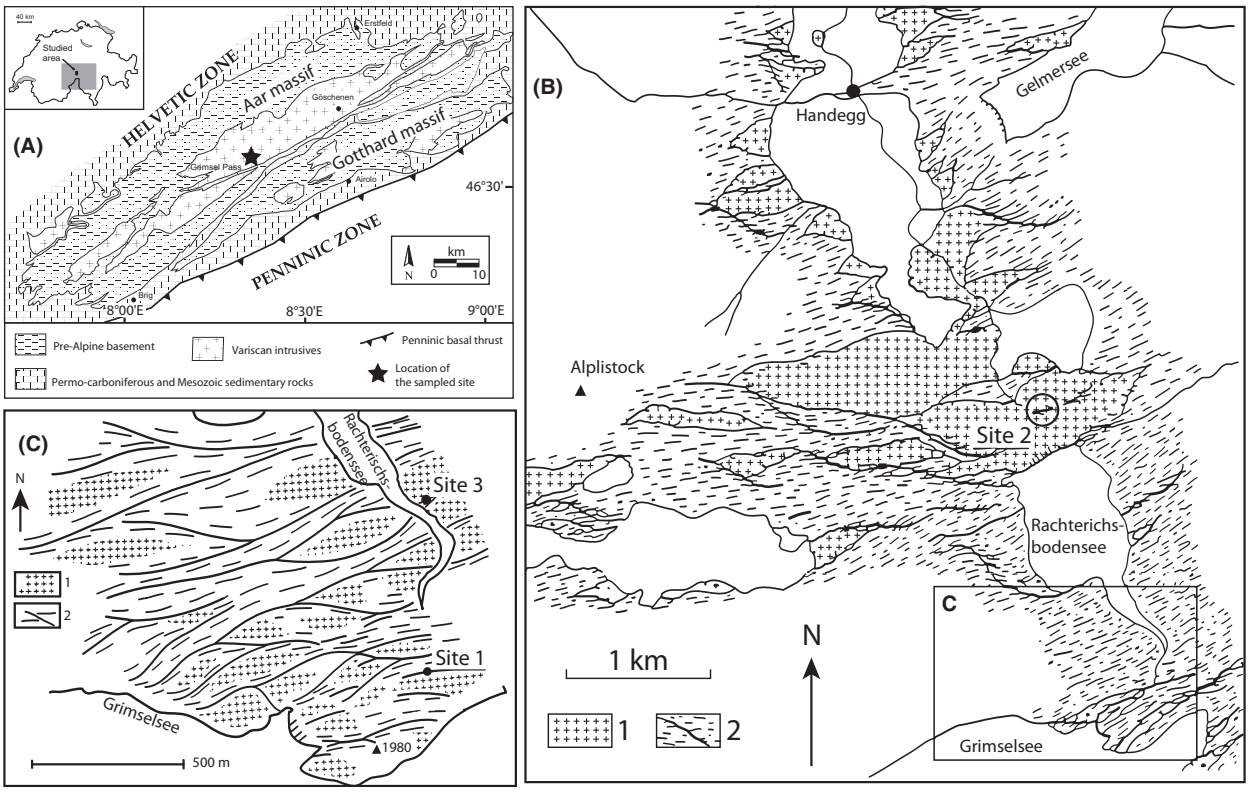

Fig. 1 (A) General geological map of the External Crystalline Massifs. (B and C) Closer-scale structural maps of the studied area showing sampling site locations (maps modified after Choukroune and Gapais (1983) and Marquer (1987)). Sites 1 and 3 are shear zones in the Grimsel granodiorite, and Site 2 is a shear zone in the Aar granite. Lithology 1 represents weakly deformed protolith areas; lithology 2 represents shear zones.

dextral strike-slip deformation (e.g. Hubbard and Mancktelow, 1992), great care was taken during sampling to avoid areas affected by these later deformation stages.

Procedures

Standard oriented palaeomagnetic cores were sampled from two sites in the Grimsel granodiorite and one site in the Aar granite. At each site, 11–13 cores were taken in 10–35-m-wide transects across exposed shear zones and classified as protolith, orthogneiss or mylonite (Fig. 2C). Anisotropy of magnetic susceptibility (AMS) was measured on all specimens using a KLY-3 Kappabridge magnetic susceptometer. AMS data were processed using the *PaleoMac* application of Cogné (2003). Additional rock magnetic characterization was performed on a vibrating sample magnetometer. The shape parameters of magnetic lineation, $L = k_1/k_2$, and magnetic foliation, $F = k_2/k_3$, were used to describe the shape of the magnetic fabric ellipsoid, where k_1, k_2 and k_3 are the maximum, intermediate and minimum principal susceptibilities respectively. The shape parameter T, defined as [ln (F) − ln (L)]/[ln (F) + ln (L)], indicates oblate or prolate fabric ellipsoids for positive or negative T values respectively. The corrected degree of anisotropy,

$$P' = \exp\sqrt{2\left[(\eta_1-\eta)^2+(\eta_2-\eta)^2+(\eta_3-\eta)^2\right]}$$

with $\eta_i = \ln (k_i)_{i=1,3}$ and $\eta = (\eta_1 + \eta_2 + \eta_3)/3$, defined by Jelinek (1981) indicates the intensity of the magnetic fabrics. Finite strain axis orientations were measured in the field using mineral stretching lineations to define the λ_1 maximal strain axis and using the schistosity as the λ_1/λ_2 finite strain plane, thus defining the λ_3 minimal strain axis as the pole to the schistosity plane. Quantitative strain estimates were made in the field by measuring the λ_1/λ_2, λ_2/λ_3 and λ_1/λ_3 finite strain ratios directly on mafic enclaves in 24 samples of weakly deformed granodiorite, orthogneisses and mylonites from shear zones located in the Grimsel granodiorite between Site 1 and Site 3 (see Marquer *et al.*, 1985; Marquer, 1989). Equivalent fabric shape and intensity parameters T^* and P^* were calculated using λ_1, λ_2 and λ_3 principal strain values in place of principal susceptibilities to describe and compare the measured strain ellipsoids with the magnetic anisotropy. Thin sections for microanalysis and optical microscopy were prepared perpendicular to the foliation and parallel to the stretching lineation. To identify opaque and accessory minerals, Raman spectroscopy was performed using a Renishaw inVia spectrometer combined with a confocal optical microscope using a 532-nm-wavelength (green) laser.

Results

Mineralogy and petrography

The Aar granite and Grimsel granodiorite are mainly composed of

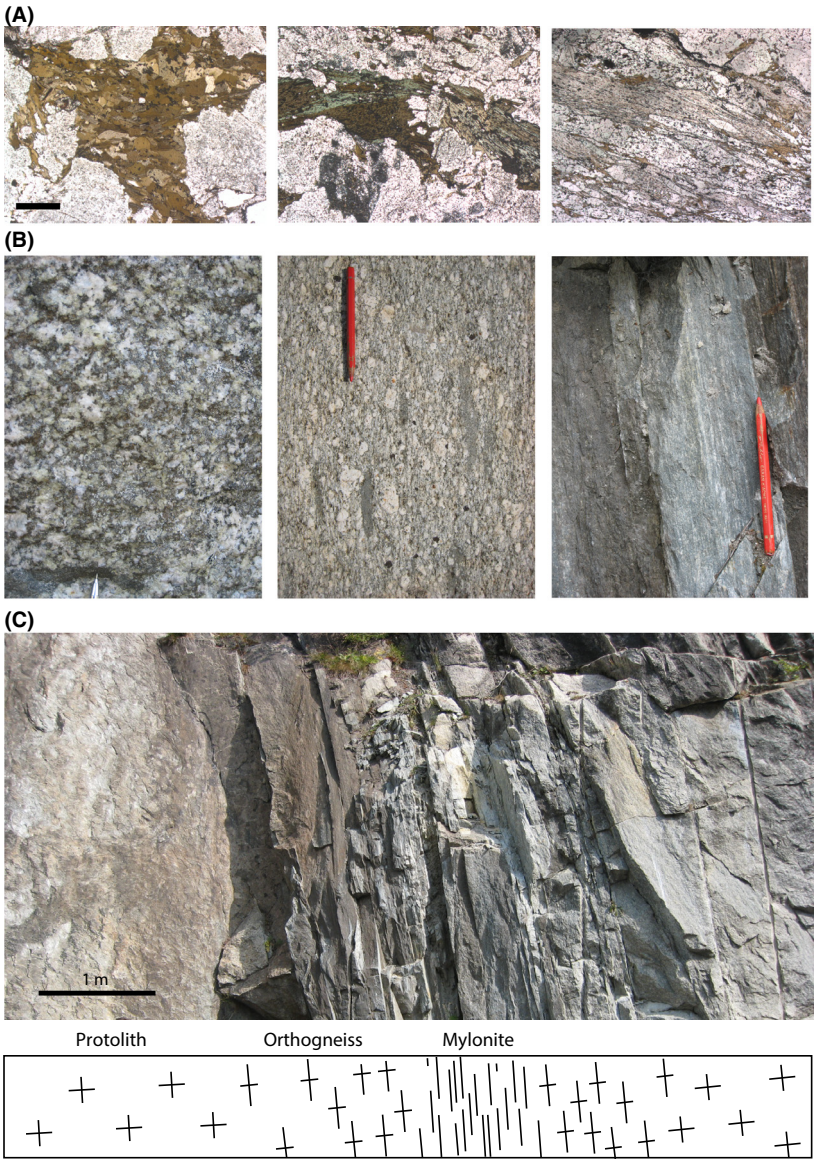

Fig. 2 Examples of structural features in ductile shear zones in the Aar Massif rocks. (A) Thin sections showing the evolution of biotite grain size and shape from magmatic biotites (left) to secondary metamorphic biotites (right) (scale bar = 500 microns). (B) Macroscopic field photos showing the large reduction in grain size between weakly deformed granite (left) and mylonite (right). (C) Outcrop photo of Site 2 showing the change in structural facies across a ductile shear zone.

quartz (30–20%), oligoclase (40–50%), K-feldspar (20–15%) and biotite-I (10–15%) (Steck, 1966). The mineralogical assemblage associated with deformation in the orthogneiss is metamorphic albite, biotite-II, phengite and epidote. In the mylonites, large fluid-related mass-transfers destabilized feldspars to produce a phengite–albite–biotite-II–chlorite–quartz mineral assemblage (Marquer *et al.*, 1985; Marquer, 1987; Goncalves *et al.*, 2012; Fig. 2A). Grain size decreased from an average of 1 mm in the weakly deformed granodiorite to about 30 μm in the mylonite (Marquer, 1987; Fig. 2B). The mineralogical and microstructural evolution from protolith to mylonite is described below.

The granitic protoliths contain indications of earlier stages of alteration and/or weak metamorphism. Plagioclase is consistently sericitized, and quartz frequently exhibits undulose extinction with occasional subgrains. Secondary biotite and magmatic epidote (allanite) are sporadically present. In orthogneisses, white mica (phengite) occurs as numerous inclusions in feldspar, and metamorphic epidote and titanite are present. Some biotite-I is still present (Fig. 2A). Plagioclase and K-feldspar exhibit brittle deformation features and are occasionally boudinaged. Abundant fine-grained bands of mica and quartz define a moderately strong schistosity. Mylonites show a strong schistosity primarily defined by white mica and biotite-II, with small bands of opaque and high-relief minerals. Abundant fine-grained albite and quartz are extensively recrystallized into fine-grained ribbons. K-feldspar is totally replaced by white mica and quartz.

Concerning accessory minerals, hysteresis loops measured on selected subsamples are essentially linear in character (Fig. 3A), indicating the absence of ferrimagnetic phases. Bulk susceptibility (k_{mean}) can be used as a rough proxy for Fe-content in paramagnetic granitoids (Bouchez *et al.*, 1990). k_{mean} values are in the range 50–500 $\times$ 10^{-6} [SI], consistent with the absence of ferrimagnetic phases and comparable to those of many phyllosilicate-dominated granitoids (e.g. Gleizes *et al.*, 1993). There is significant k_{mean} variability within and between sites (Fig. 3B, Table 2), and occasionally within cores, indicating some degree of heterogeneity in the abundance of Fe-bearing phases. In Raman spectra from all samples, opaque and accessory phases largely correspond to rutile with some titanite, with ilmenite additionally identified only in Site 1 samples (Fig. 3C). Small amounts of ilmenite may account for the overall higher k_{mean} values at Site 1 (Table 2), as was determined for gneissic mylonites by Siegesmund *et al.* (1995). From these analyses, we conclude that biotite is likely the dominant AMS-carrier in all samples, while synkinematically produced phengite (Fe–Mg-bearing white mica, see Challandes *et al.*,

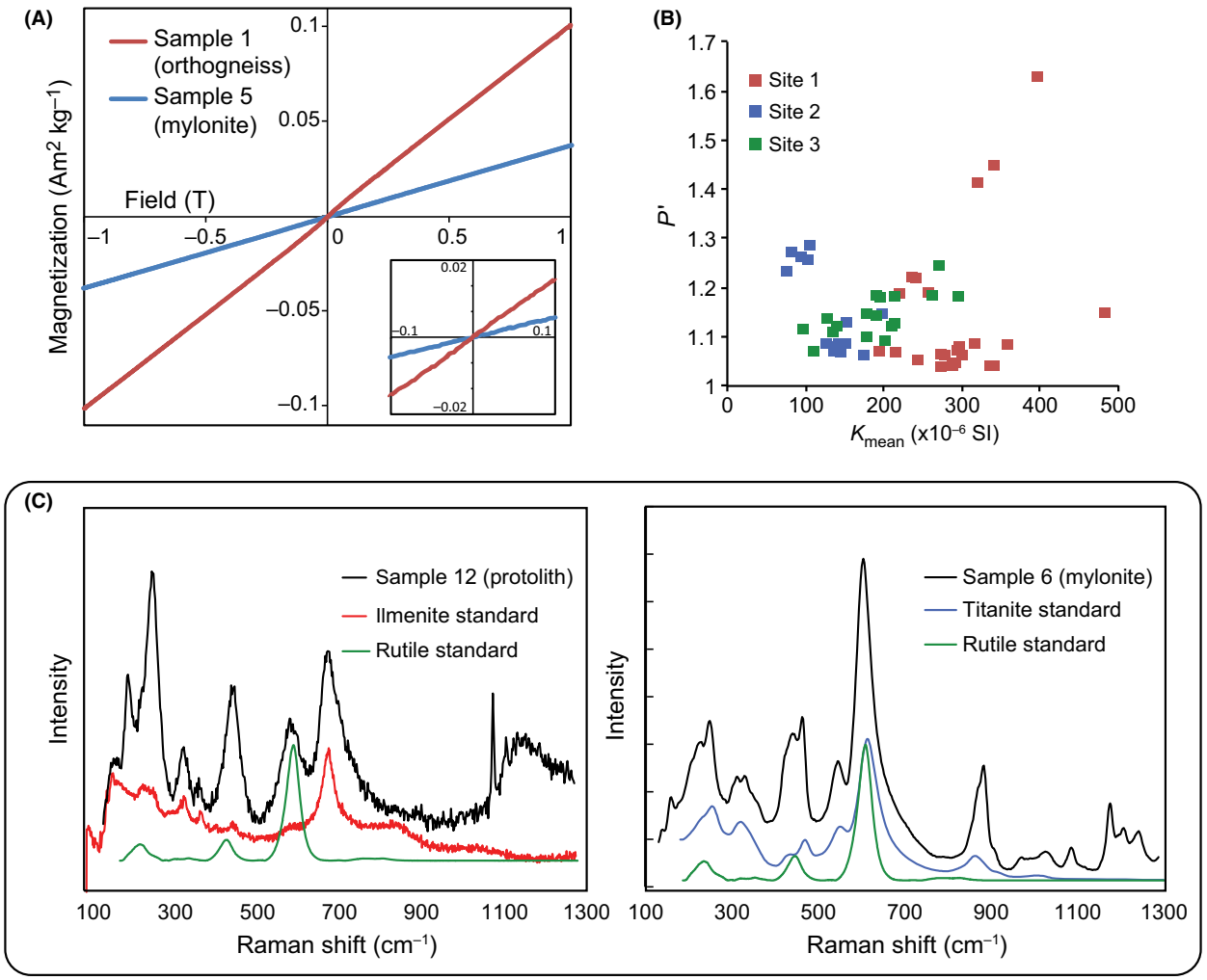

Fig. 3 Results of magnetic and opaque mineral characterization from samples from Site 1. (A) Representative hysteresis loops for an orthogneiss (sample 1) and a mylonite (sample 5). Inset: detailed plot of centre portions from the hysteresis loops. (B) Bulk susceptibility (k_{mean}) plotted against P' for samples from each site. (C) Raman spectra for opaque minerals from a granodiorite protolith (sample 12) and a mylonite (sample 6) compared with Raman spectra from ilmenite, rutile and titanite standards.

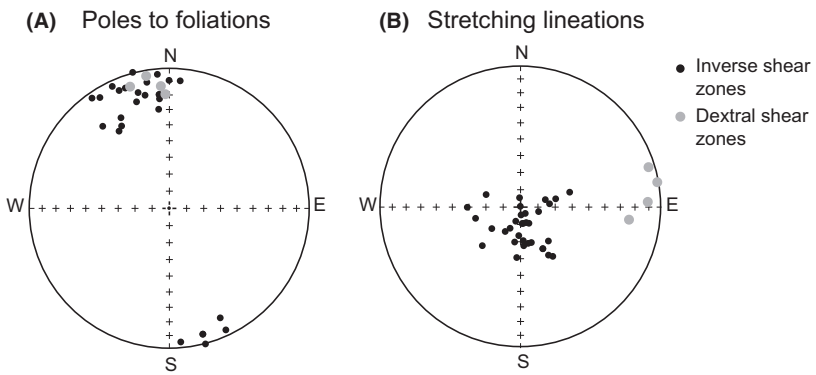

Fig. 4 Stereoplots of structural orientations measured in the field. (A) Poles to schistosity ($\lambda_1\lambda_2$ plane) and (B) stretching lineations (λ_1) for inverse (black symbols, site 3) and dextral (grey symbols, site 1) shear zones in the Grimsel granodiorite. The plots are equal-area projections onto the lower hemisphere.

Table 1 Strain data measured on mafic enclaves in the Grimsel granodiorite, orthogneisses and mylonites (Marquer, 1987, 1989). The finite strain parameters are defined in the text.

Sample	Facies	λ_1/λ_2	λ_2/λ_3	λ_1/λ_3	T^*	P^*
AD 26	p	1.16	1.2	1.39	0.103	1.39
AD 27	p	1.1	1.4	1.54	0.559	1.59
AD 28	p	1.12	1.56	1.75	0.594	1.82
AD 15	p	1.42	3.16	4.49	0.533	5.12
AD 13	p	1.58	3	4.74	0.412	5.32
AD 11	p	2.07	2.55	5.28	0.125	5.75
AD 2	o	1.76	3.1	5.46	0.334	6.10
AD 6	o	1.7	3.6	6.12	0.414	6.97
AD 18	o	1.68	3.7	6.22	0.432	7.28
AD 12	o	1.71	4.07	6.96	0.447	8.21
AD 14	o	1.76	4.99	8.78	0.480	11.19
AD 3	o	1.79	5.46	9.77	0.489	12.31
AD 10	o	1.92	6.21	11.91	0.474	15.74
AD 1	o	2.42	5.96	14.42	0.338	18.98
AD 22	o	1.88	6.68	12.56	0.501	16.97
AD 17	o	2.06	6.62	13.64	0.447	18.90
AD 16	m	2.75	6.33	17.42	0.292	24.00
AD 7	m	2.13	7.49	15.95	0.454	23.04
AD 19	m	2.5	8.35	20.88	0.397	30.88
AD 25	m	2.86	8.05	23.02	0.330	33.50
AD 5	m	1.89	9.29	17.56	0.556	27.07
AD 29	m	1.65	18.68	30.75	0.708	76.32
AD 20	m	1.64	21.35	35.01	0.722	71.17
AD 21	m	4.03	19.67	79.27	0.363	164.83

p, protolith; o, orthogneiss; m, mylonite.

2008) will additionally contribute to AMS strength in mylonites and orthogneisses, as will minor ilmenite at Site 1.

Finite strain estimates and field structures

Following the strain pattern analysis of Gapais *et al.* (1987) (see their figure 10), the sampled vertical shear zones at Sites 2 and 3 have directions close to the main regional N70 schistosity, with vertical mineral stretching lineations in the mylonite zones (Fig. 4). At Site 1, the direction of the vertical shear zone is N80–90 with a dextral shearing component in the mylonites associated with local horizontal mineral stretching lineations (grey dots in Fig. 4B).

The shapes of the strain ellipsoids calculated from strain markers in the Grimsel granodiorite are generally oblate, with T^* around 0.1–0.7. The finite strain ratios (λ_1/λ_3) reach as high as 80 (Table 1), while the P^* values of strain intensity, which account for the triaxial nature of the strain ellipsoid, are extremely large in the mylonites, reaching over 160 (Fig. 5A).

AMS results

Magnetic fabric shapes are predominantly oblate with significantly higher fabric intensities in mylonites than in protolith or orthogneisses. The AMS fabric shapes from Site 1 closely follow those of the strain ellipsoids (compare Fig. 5A and B). AMS intensities are highest at Site 1, the southernmost site, consistent with the previously observed pattern of southwardly increasing regional deformation intensity in the Aar Valley (Choukroune and Gapais 1983).

Protolith AMS is moderately strong, with P' ranging from 1.038 to 1.126 (Table 2). In contrast, AMS intensities for biotite-dominated magmatic fabrics in granite typically reach only 1.05 (e.g. Bouillin *et al.*, 1993). Magnetic fabrics in samples identified as orthogneiss are not significantly stronger than in protolith samples. The orthogneiss P' range of 1.051–1.182 overlaps considerably with that of protolith samples, and the mean orthogneiss AMS intensity at Site 2 is actually lower than that of the protolith (Fig. 5B, inset). As expected, mylonitic samples have the strongest magnetic fabrics, with P'

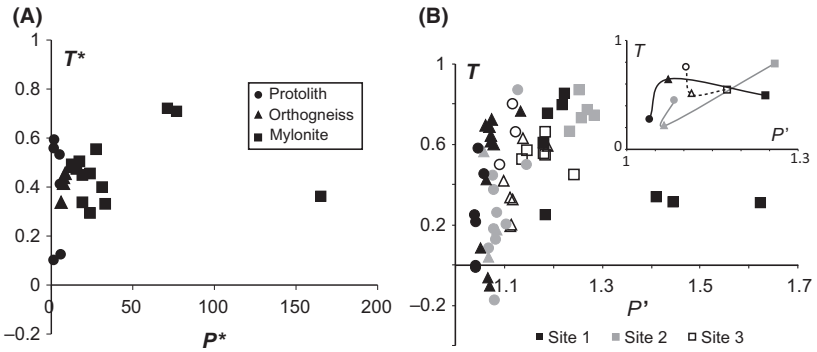

Fig. 5 Plots of fabric shape parameters (T, T^*) vs. fabric intensity (P', P^*). (A) Variation in shape as a function of strain intensity for strain markers measured in the Grimsel granodiorite. (B) Variation in the AMS ellipsoid shape as a function of degree of anisotropy for different sites and facies. The inset plot in (B) shows mean values for each facies at each site.

Table 2 AMS shape, intensity and orientation parameters at the three studied sites. The anisotropy parameters are defined in the text.

Name	Facies	Distance (m)	k_{mean} (× 10^{-6} SI)	*L*	*F*	*P′*	*T*	$k1_{dec}$	$k1_{inc}$	$k2_{dec}$	$k2_{inc}$	$k3_{dec}$	$k3_{inc}$
Site 1 (46°34.5′N, 8°20.1′E)													
AAR01A	o	10.3	285.8	1.014	1.06	1.079	0.622	171.9	24.1	346.1	65.8	81	2.2
AAR01B	o	10.3	299.5	1.012	1.061	1.079	0.657	174.1	40.2	0.2	49.6	266.6	3
AAR01C	o	9.1	319.2	1.015	1.063	1.084	0.604	174.6	37.5	0.7	52.4	266.9	2.9
AAR02A	o	9.1	360.9	1.011	1.065	1.082	0.713	154.5	35.6	323.2	53.9	60.6	5.4
AAR03A	o	8.1	280.1	1.009	1.048	1.061	0.691	186.5	29	1.2	60.9	95.2	2.2
AAR03B	o	8.1	275.5	1.018	1.044	1.064	0.421	188.6	35.9	355	53.3	93.8	6.5
AAR03C	o	8.1	296.4	1.01	1.056	1.071	0.694	183.6	24.8	4.1	65.2	273.6	0.2
AAR04A	m	7.55	217.0	1.035	1.031	1.067	−0.062	344	3.6	234.8	79.3	74.7	10.1
AAR04B	m	7.55	197.1	1.038	1.03	1.069	−0.112	351.1	3.6	140.8	85.8	260.9	2.1
AAR05A	m	7.3	343.0	1.132	1.268	1.444	0.313	340.3	31.7	170.5	57.8	73.1	4.6
AAR05B	m	7.3	323.2	1.117	1.254	1.41	0.341	333.4	34.5	164.1	55	66.9	5
AAR06A	m	7.25	244.1	1.017	1.174	1.217	0.808	347	57.1	180.6	32.2	86.7	6.2
AAR06B	m	7.25	237.9	1.013	1.179	1.219	0.855	354.6	56.6	176.7	33.4	86.1	1
AAR07A	m	7.2	399.0	1.179	1.366	1.623	0.308	10.2	73.3	179.9	16.5	270.7	2.8
AAR07B	m	7.2	259.2	1.02	1.15	1.189	0.757	331.9	62.1	165.8	27.2	72.8	5.7
AAR08A	m	7.17	223.3	1.032	1.136	1.184	0.604	331.5	47.1	182.5	38.5	79.4	15.9
AAR09A	o	5.6	246.4	1.023	1.027	1.051	0.083	149.4	45.3	253.6	13.6	356	41.5
AAR09B	o	5.6	485.0	1.015	1.117	1.146	0.768	237.4	27.9	131.6	27.3	5	49.1
AAR10A	p	0.3	275.6	1.014	1.023	1.038	0.251	153.3	1.4	61.9	44.2	244.7	45.8
AAR11A	p	0.2	339.2	1.016	1.024	1.041	0.217	154	13.2	39.7	60.4	250.5	26
AAR11B	p	0.2	343.1	1.02	1.02	1.04	−0.002	152.6	12.6	43.3	55.9	250.4	31.1
AAR11C	p	0.2	304.1	1.015	1.042	1.06	0.455	149.9	20.9	33.4	49.5	254.2	32.9
AAR12A	p	0	294.9	1.009	1.034	1.045	0.587	184	10.8	81.9	47.5	283.4	40.4
AAR12B	p	0	291.1	1.02	1.02	1.04	−0.015	179.7	2.4	86.4	53.3	271.5	36.5
Site 2 (46°35.5′N, 8°19.4′E)													
AAR14A	m	35.1	96.1	1.028	1.201	1.258	0.735	160.1	10.9	38.5	69.7	253.5	16.8
AAR15A	m	35	85.1	1.025	1.213	1.27	0.775	349.6	3.5	88.4	68	258.2	21.7
AAR15B	m	35	106.2	1.013	1.209	1.254	0.871	348.9	7.4	98.6	68.9	256.3	19.7
AAR16A	m	34.76	76.9	1.033	1.176	1.231	0.669	357.6	15	120.8	63.9	261.7	20.8
AAR17A	m	34.2	107.8	1.029	1.222	1.283	0.752	171	9.9	54.3	68.8	264.3	18.6
AAR18A	o	33.4	129.0	1.035	1.049	1.086	0.17	352.6	0.8	87.3	80.4	262.5	9.6
AAR19A	o	32.6	138.9	1.032	1.036	1.069	0.045	340.1	3.5	78.5	67.6	248.7	22.1
AAR20A	p	32	107.7	1.023	1.052	1.079	0.385	350.4	23.5	124.6	58	251.1	20.4
AAR20B	p	32	132.2	1.039	1.06	1.103	0.207	131.3	42.8	349.3	40.4	241.1	20.1
AAR21A	o	31	176.6	1.012	1.044	1.06	0.567	331.4	0.1	61.6	61.5	241.3	28.5
AAR22A	p	19	154.3	1.007	1.104	1.126	0.87	152.1	19.9	352.9	68.9	244.6	6.9
AAR22B	p	19	145.2	1.02	1.053	1.077	0.451	160.3	6.4	54.8	67.1	252.9	21.9
AAR22C	p	19	142.3	1.032	1.047	1.08	0.184	167	31.7	343.4	58.3	76	1.6
AAR23A	p	5	143.7	1.03	1.052	1.084	0.265	165.7	18.1	51.1	51.8	267.6	32.3
AAR23B	p	5	148.3	1.035	1.046	1.083	0.129	357.8	11.3	101.9	50.6	259.1	37.2
AAR23C	p	5	200.6	1.033	1.103	1.146	0.502	3.8	11.3	107.8	50.4	265	37.3
AAR24A	p	0	140.5	1.045	1.032	1.079	−0.173	165.1	8.4	52.8	68.7	258.1	19.4
AAR24B	p	0	147.5	1.03	1.036	1.066	0.091	333	2.9	70	67.5	241.9	22.3
Site 3 (46°34.8′N, 8°20.0′E)													
AAR26A	o	9.5	98.8	1.043	1.066	1.113	0.203	187.4	0.7	92.8	80.8	277.6	9.2
AAR27A	m	9.35	198.2	1.03	1.131	1.176	0.608	1.5	2.2	184.9	87.8	91.5	0.1
AAR27B	m	9.35	130.2	1.029	1.098	1.136	0.524	184	5.5	314	81.4	93.3	6.5
AAR28A	m	9.3	180.9	1.028	1.107	1.146	0.57	1.1	2.3	130.3	86.3	270.9	2.9
AAR28B	m	9.3	216.0	1.035	1.131	1.18	0.564	359.1	0.9	136.6	88.7	269.1	0.9
AAR29A	m	9.2	298.1	1.026	1.138	1.181	0.665	179.2	4.5	70.8	76	270.2	13.2
AAR30A	m	9.1	264.5	1.036	1.132	1.182	0.552	176.5	2.4	47.1	86.2	266.6	2.9
AAR30B	m	9.1	272.9	1.06	1.165	1.243	0.449	354.6	2.2	103.5	83.2	264.4	6.5
AAR31A	o	8.75	141.4	1.038	1.075	1.118	0.325	189.2	12.1	42.2	75.7	280.8	7.6
AAR31B	o	8.75	137.6	1.034	1.07	1.109	0.341	192.8	11	40.2	77.6	283.9	5.6
AAR32A	o	8.3	112.8	1.038	1.031	1.07	−0.104	184.9	12.2	40.7	75.1	276.7	8.5
AAR33A	o	7.3	180.8	1.026	1.066	1.097	0.426	188	43.5	16.5	46.1	282	4.3
AAR34A	o	3	192.7	1.03	1.136	1.182	0.623	196.9	0.2	97.9	88.9	286.9	1.1
AAR34B	o	3	193.7	1.023	1.105	1.139	0.636	198.2	33.9	22.2	56	289.5	1.8

Table 2 (Continued).

Name	Facies	Distance (m)	k_{mean} (× 10^{-6} SI)	*L*	*F*	*P′*	*T*	$k1_{dec}$	$k1_{inc}$	$k2_{dec}$	$k2_{inc}$	$k3_{dec}$	$k3_{inc}$
AAR35A	p	0.5	216.1	1.019	1.096	1.125	0.665	11.6	27.6	204.4	61.8	104.4	5.4
AAR36A	p	0	203.9	1.021	1.065	1.091	0.499	216.6	20.4	34.8	69.6	126.4	0.6
AAR36B	p	0	211.8	1.01	1.096	1.118	0.802	216.7	9.2	34.1	80.8	126.6	0.4

p, protolith; o, orthogneiss; m, mylonite.

values ranging from 1.067 to 1.623. The P' values of the mylonite samples are large considering that the degree of magnetic anisotropy for individual phyllosilicate grains generally ranges between 1.1 and 1.7 (Hrouda, 1993), with average values for biotite crystals of around 1.3 (Martín-Hernández & Hirt 2003). No systematic correlation is seen between P' and k_{mean} values (Fig. 3B), indicating little compositional influence on AMS.

P' profiles across the three site transects (Fig. 6A) demonstrate that, while mylonite samples exhibit clearly elevated fabric intensities, the degree of anisotropy does not vary as a simple function of proximity to mylonite centres. The variation in fabric shape represented by T values is even more pronounced. In contrast, values of finite strain increase progressively from the protolith to the mylonites (Fig. 6B). All sites exhibit weak P' minima and strong local decreases in T in orthogneisses adjacent to the mylonitic zones. Potential origins of this pattern are proposed in the Discussion.

k_{min} axes (poles to magnetic foliation) for all sites are nearly horizontal and strongly clustered around the NNW–SSE axis, delineating a consistently subvertical magnetic foliation plane striking ENE–WSW (Fig. 7). k_{max} axes (magnetic lineations) are subvertical in all samples except for mylonites at Site 1, where k_{max} lies along the horizontal axis in the foliation plane, with k_{int} parallel to the vertical axis, consistent with the horizontal stretching lineations observed in outcrops. The AMS ellipsoid orientations for all sites and facies plotted together in Fig. 8 in comparison with measured field structure orientations show remarkably good agreement between the magnetic fabric directions and the principal strain directions.

Discussion

Although macroscopic fabrics in the protolith are weak (Fig. 2B), AMS measurements indicate that there is a moderately strong mineral shape anisotropy. The protolith anisotropy likely results from a synemplacement Variscan magmatic petrofabric, possibly with a minor influence of weak penetrative ductile deformation. Oliva-Urcia *et al.* (2012) reported comparably strong granite emplacement fabrics for biotite-carried AMS.

The horizontal outcrop stretching lineations and k_1 magnetic anisotropy axes oriented N80–90, indicating local dextral movement, in mylonites at Site 1 belong to the conjugate structures in the Aar Massif identified by Choukroune and Gapais (1987), which accommodate local intermediate extension along the horizontal bulk λ_2 strain axis. Minor horizontal extension in addition to major subvertical extension is consistent with the dominantly co-axial nature of Alpine bulk shortening deformation and oblate finite strain.

Although Alpine deformation in the Aar Massif was accompanied by significant synkinematic mass-transfer and fluid interaction, Goncalves *et al.* (2012) report only small decreases in Fe in strongly deformed rocks and constant relative proportions of biotite during metamorphism. Variations in AMS properties are thus not affected by the growth or breakdown of Fe-oxides and should reflect the behaviour of phyllosilicate minerals during deformation and metamorphism. Several studies have found discrepancies between phyllosilicate-carried AMS fabrics and phyllosilicate crystallographic textures. Oliva-Urcia *et al.* (2012) determined that AMS represents composite fabrics created by the spatial distribution of particles, rather than the orientations of individual grains. High P' values in our samples may therefore reflect the highly anisotropic spatial distribution of mica in the mylonites as they develop into banded polycrystalline arrangements.

Similarly, Siegesmund *et al.* (1995) reported that, while the measured AMS orientations matched well with those modelled from mica textures, discrepancies arose between the T and P' parameters due to girdling of mica around silicate porphyroclasts. Aggregates of phyllosilicates may thus produce magnetic fabrics that differ from those of individual grains. Such mechanisms may be the source of magnetic lineations in the Aar Massif samples, as has been demonstrated for the subparallel alignment of biotite crystals along zone axes (Kruckenberg *et al.*, 2010). O'Brien *et al.* (1987) determined that progressive deformation in mylonite zones produces a 'steady state' foliation fabric in phyllosilicates, resulting in AMS saturating at P' values around 1.2 (Siegesmund *et al.*, 1995). These P' values occur only in Aar Massif mylonites, therefore it is possible that relative strain within the mylonite zones is not represented by AMS fabrics.

The local decreases in P' and T in orthogneisses relative to the mylonites and protolith (Fig. 5) probably reflect the growth of large quantities of white mica during syn-deformational metamorphism (Goncalves *et al.*, 2012). Although white micas have lower susceptibilities than biotite, Martín-Hernández and Hirt (2003) reported similar crystalline anisotropies for muscovite, suggesting that the Fe-bearing phengite in deformed Aar rocks may contribute to the AMS. In the orthogneisses, neoformation of white mica occurs as inclusions in and around altered feldspar grains, which initially

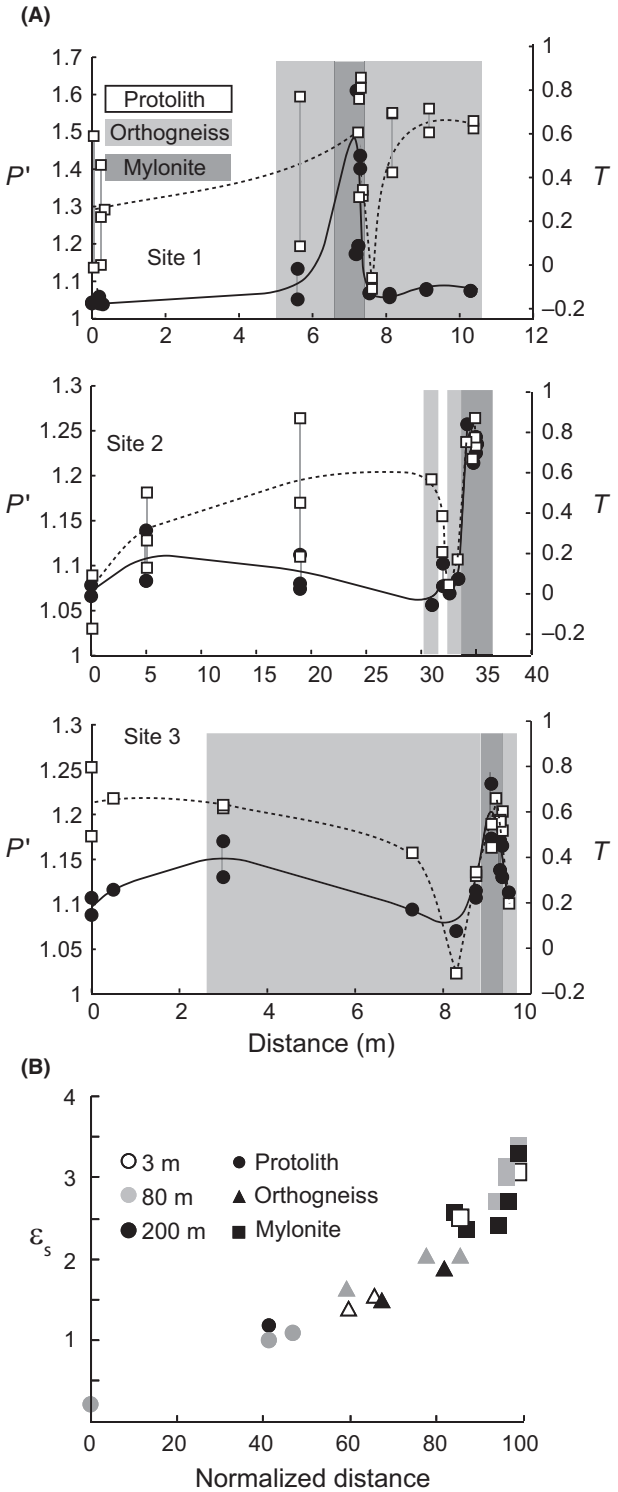

Fig. 6 (A) Profiles of P' (circles and solid lines) and shape parameter T (squares and dashed lines) across the sampled shear-zone transects at each studied site, demonstrating the patterns of magnetic anisotropy variation with deformation. (B) Finite strains measured on mafic enclaves across shear zones of varying widths (represented by different symbols) in the Grimsel granodiorite plotted as a function of normalized distance from the mylonite centres.

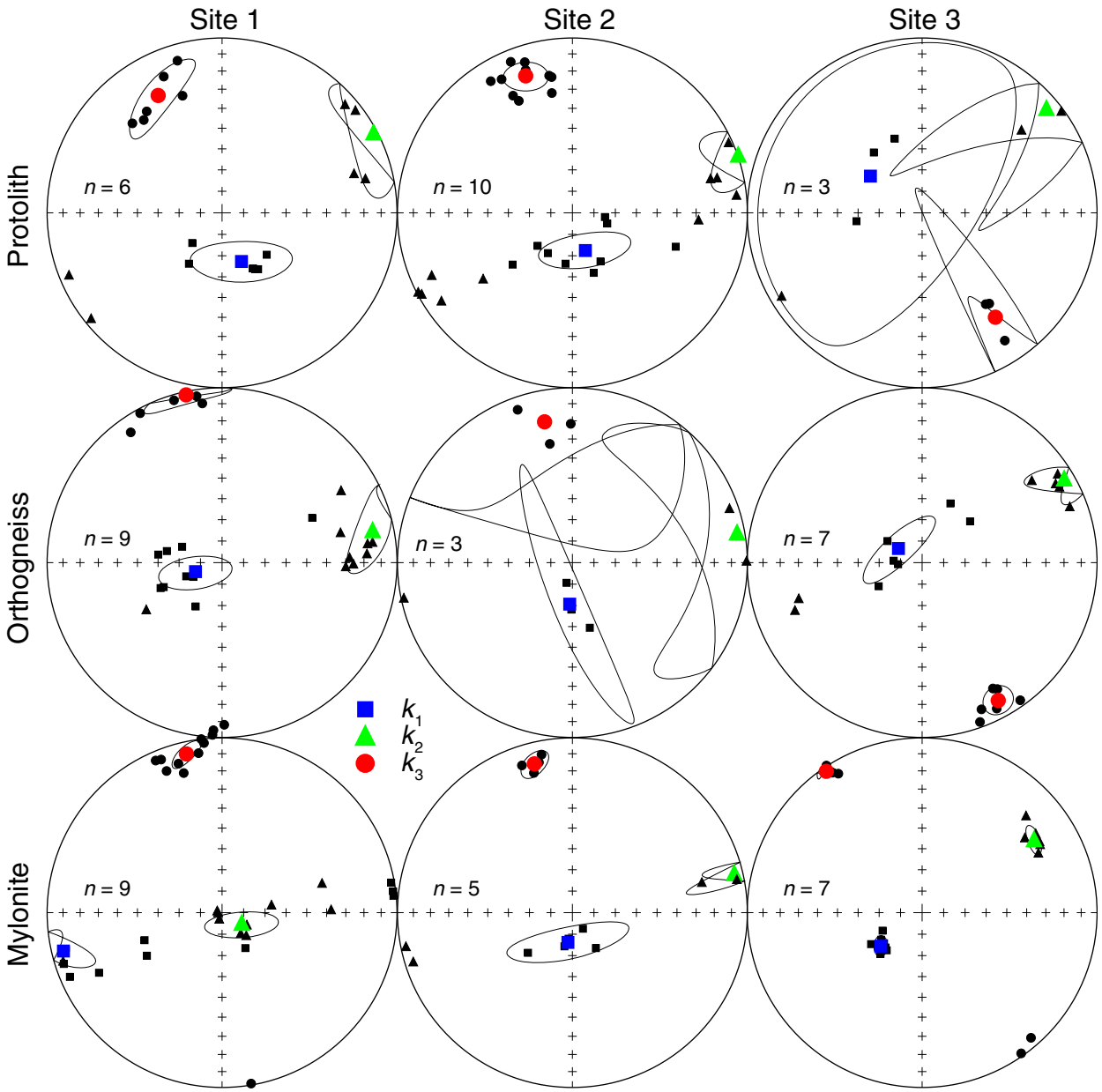

Fig. 7 Stereoplots representing AMS principal susceptibility axes by site (columns) and sample type (e.g. protolith, orthogneiss and mylonite; rows). Squares: maximum (k_1), triangles: intermediate (k_2) and circles: minimum (k_3) susceptibility axes. Large coloured symbols are mean AMS tensor eigenvectors (Jelinek, 1978) with their 95% confidence ellipses. All plots are equal-area projections onto the lower hemisphere. Note the horizontal mean k_1 in Site 1 mylonites (see text for explanation).

behave as rigid porphyroclasts. Thus, the growth of randomly oriented white mica inclusions in the orthogneisses should weaken the AMS intensity and produce less-oblate fabric shapes. Complete breakdown and recrystallization of feldspar in the mylonites results in the rearrangement of mica into elongated bands, reflected by high AMS intensities.

Conclusions

Magnetic fabric analysis was performed in synkinematically metamorphosed ductile Alpine shear zones in the Aar Massif. Excellent agreement exists between finite strain and magnetic anisotropy principal axis orientations. The magnitudes and shapes of magnetic fabrics exhibit local variations independent of strain, which likely reflect new growth of phyllosilicates during fluid-present deformation. Subvertical magnetic lineations corresponding to the observed vertical stretching lineation and subhorizontal minimum magnetic and finite strain axes parallel the Tertiary Alpine compression oriented NNW–SSE in this part of the Aar Massif.

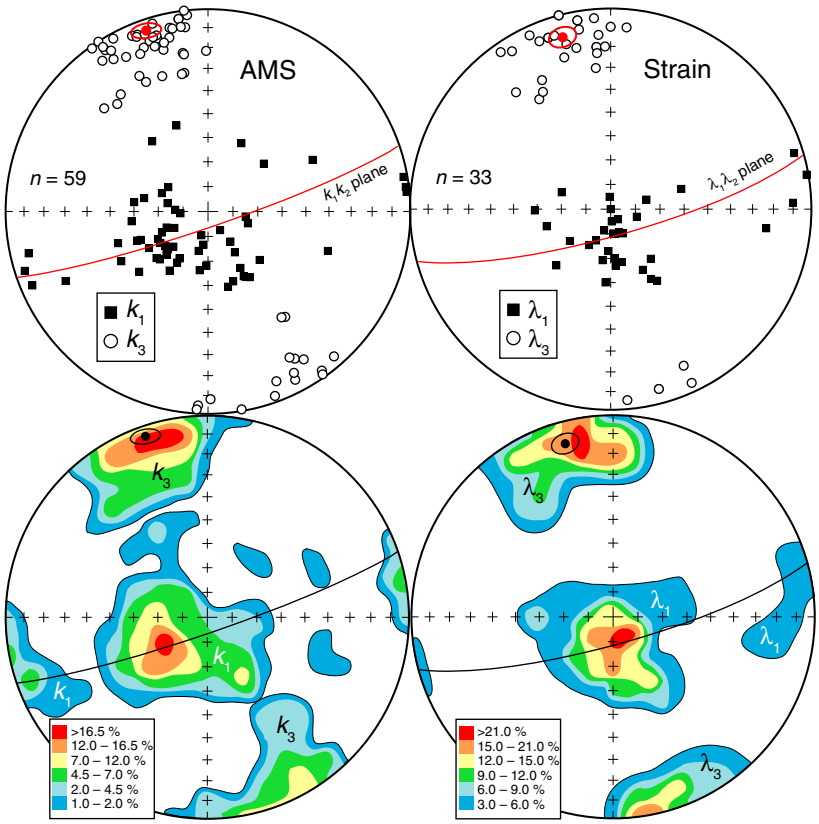

Fig. 8 Comparison of AMS and strain principal axes. Top: maximum (k_1 and λ_1; black squares) and minimum (k_3 and λ_3; open circles) axes of AMS (left) and strain (right) tensors; mean magnetic (k_1k_2) and macroscopic ($\lambda_1\lambda_2$) foliation planes together with their poles (k_3, λ_3) and their 95% confidence areas. Bottom: Density plots of these distributions in the lower hemisphere; contours are given as the percentage of data in 1% of the hemisphere surface.

Acknowledgements

We thank Associate Editor Mark Dekkers and three anonymous reviewers for their helpful and constructive comments.

References

Abrecht, J., 1994. Geologic units of the Aar Massif and their pre-Alpine rock associations; a critical review. The pre-Alpine crustal evolution of the Aar, Gotthard and Tavetsch massifs. *Schweiz. Mineral. Petrogr. Mitt.*, **74**, 5–27.

Borradaile, G.J. and Jackson, M., 2004. Anisotropy of magnetic susceptibility (AMS): magnetic petrofabrics of deformed rocks. *Geol. Soc. London Spec. Publ.*, **238**, 299–360.

Bouchez, J.L., Gleizes, G., Djouadi, T. and Rochette, P., 1990. Microstructure and magnetic susceptibility applied to emplacement kinematics of granites: the example of the Foix pluton (French Pyrenees). *Tectonophysics*, **184**, 157–171.

Bouillin, J.P., Bouchez, J.L., Lespinasse, P. and Pecher, A., 1993. Granite emplacement in an extensional setting: an AMS study of the magmatic structures of Monte Capanne (Elba, Italy). *Earth Planet. Sci. Lett.*, **118**, 263–279.

Challandes, N., Marquer, D. and Villa, I.M., 2008. PTt modelling, fluid circulation, and 39Ar-40Ar and Rb-Sr mica ages in the Aar Massif shear zones (Swiss Alps). *Swiss J. Geosci.*, **101**, 269–288.

Choukroune, P. and Gapais, D., 1983. Strain pattern in the Aar Granite (Central Alps); orthogneiss developed by bulk inhomogeneous flattening. *J. Struct. Geol.*, **5**, 411–418.

Cogné, J.P., 2003. PaleoMac: a Macintosh™ application for treating paleomagnetic data and making plate reconstructions. *Geochem. Geophys. Geosyst.*, **4**, 1007.

Ferré, E.C., Gébelin, A., Till, J.L., Sassier, C. and Burmeister, K.C., 2014. Deformation and magnetic fabrics in ductile shear zones: a review. *Tectonophysics*, **629**, 179–188.

Fourcade, S., Marquer, D. and Javoy, M., 1989. $^{18}O/^{16}O$ variations and fluid circulation in a deep shear zone: the case of the Alpine ultramylonites from the Aar Massif (Central Alps, Switzerland). *Chem. Geol.*, **77**, 119–131.

Gapais, D., Bale, P., Choukroune, P., Cobbold, P.R., Mahjoub, Y. and Marquer, D., 1987. Bulk kinematics from shear zone patterns; some field examples. *J. Struct. Geol.*, **9**, 635–646.

Gleizes, G., Nédélec, A., Bouchez, J.L., Autran, A. and Rochette, P., 1993. Magnetic susceptibility of the Mont-Louis Andorra ilmenite-type granite (Pyrenees): a new tool for the petrographic characterization and regional mapping of zoned granite plutons. *J. Geophys. Res. Solid Earth*, **98**(B3), 4317–4331.

Goncalves, P., Oliot, E., Marquer, D. and Connoly, J.A.D., 2012. Role of chemical processes on shear zone formation: an example from the Grimsel metagranodiorite (Aar Massif, Central Alps). *J. Metamorph. Geol.*, **30**, 703–722.

Goncalves, P., Marquer, D., Oliot, E. and Durand, C., 2013. Thermodynamic modeling and thermobarometry of

rocks. In *Metasomatism and the Chemical Transformation of Rock: The Role of Fluids in Terrestrial and Extraterrestrial Processes* (D.E. Harlov and A. Austrheim, eds) *Lect. Notes in Earth Syst. Sci.*, **VI**, 800p., Springer.

Graham, J. 1966. Significance of magnetic anisotropy in Appalachian sedimentary rocks. In *The Earth Beneath the Continents* (J. Steinhart and T. Smith, eds). *Geophys. Monogr. Ser.*, **10**, 627–648. AGU, Washington, DC.

Hrouda, F., 1993. Theoretical models of magnetic anisotropy to strain relationship revisited. *Phys. Earth Planet. Inter.*, **77**, 237–249.

Hubbard, M. and Mancktelow, N.S., 1992. Lateral displacement during Neogene convergence in the western and central Alps. *Geology*, **20**, 943–946.

Jelinek, V., 1978. Statistical processing of anisotropy of magnetic susceptibility measured on groups of specimens. *Stud. Geophys. Geod.*, **22**, 50–62.

Jelinek, V., 1981. Characterization of the magnetic fabric of rocks. *Tectonophysics*, **79**, T63–T67.

Kruckenberg, S.C., Ferré, E.C., Teyssier, C., Vanderhaeghe, O., Whitney, D.L., Seaton, N.C. and Skord, J.A., 2010. Viscoplastic flow in migmatites deduced from fabric anisotropy: an example from the Naxos dome, Greece. *J. Geophys. Res. Solid Earth*, **115**(B9), B09401.

Marquer, D. 1987. Transfert de matière et déformation progressive des granitoïdes. Exemple des massifs de l'Aar et du Gothard (Alpes centrales suisses). PhD thesis, Mem. Doc. CAESS Rennes, 10, 250 pp.

Marquer, D., 1989. Transfert de matière et déformation des granitoïdes: aspects méthodologiques. *Schweiz. Mineral. Petrogr. Mitt.*, **69**, 13–33.

Marquer, D., 1990. Structures et déformation alpine dans les granites hercyniens du massif du Gothard (Alpes centrales suisses). *Eclogae Geol. Helv.*, **83**, 77–97.

Marquer, D. and Gapais, D., 1985. Les massifs cristallins externes sur une transversale Guttanen-val Bedretto (Alpes centrales): structures et histoire cinématique. *CR Acad. Sci. Paris*, t.301, Série II, **8**, 543–546.

Marquer, D. and Peucat, J.J., 1994. Rb-Sr systematics of recrystallized shear zones at the green-schist-amphibolite transition: examples from granites in the Swiss Central Alps. *Schweiz. Mineral. Petrogr. Mitt.*, **74**, 343–358.

Martín-Hernández, F. and Hirt, A.M., 2003. The anisotropy of magnetic susceptibility in biotite, muscovite and chlorite single crystals. *Tectonophysics*, **367**, 13–28.

O'Brien, D.K., Wenk, H.R., Ratschbacher, L. and You, Z., 1987. Preferred orientation of phyllosilicates in phyllonites and ultramylonites. *J. Struct. Geol.*, **9**, 719–730.

Oliva-Urcia, B., Casas, A.M., Ramón, M.J., Leiss, B., Mariani, E. and Román-Berdiel, T., 2012. On the reliability of AMS in ilmenite-type granites: an insight from the Marimanha pluton. *Central Pyrenees. Geophysical Journal International*, **189** (1), 187–203.

Pfiffner, O.A., Frei, W., Valasek, P., Stäuble, M., Levato, L., DuBois, L. and Smithson, S.B., 1990. Crustal shortening in the Alpine Orogen: Results from deep seismic reflection profiling in the eastern Swiss Alps, Line NFP 20-east. *Tectonics*, **9**, 1327–1355.

Schaltegger, U., 1994. Unravelling the pre-Mesozoic history of Aar and Gotthard Massifs (Central Alps) by isotopic dating; a review. *Schweiz. Mineral. Petrogr. Mitt.*, **74**, 41–51.

Siegesmund, S., Ullemeyer, K. and Dahms, M., 1995. Control of magnetic rock fabrics by mica preferred orientation: a quantitative approach. *J. Struct. Geol.*, **17**, 1601–1613.

Steck, A., 1966. Petrographische und tektonische Untersuchungen am zentralen Aaregranit und seinen altkristallinen Huellgesteinen im westlichen Aarmassiv im Gebiet Belalp-Grisighorn. *Beitr. Geol. Karte Schweiz.*, **130**, 96.

Steck, A., 1984. Structures et déformations tertiaires dans les Alpes Centrales (transversale Aar-Simplon-Ossola); Tertiary structures and deformation in the Central Alps, Aar-Simplon-Ossola transverse. *Eclogae Geol. Helv.*, **77**, 55–100.

Tarling, D.H. and Hrouda, F., 1993. *The Magnetic Anisotropy of Rocks*. Chapman and Hall, London.

Received 2 October 2014; revised version accepted 24 February 2015

